J. Fluid Mech. (2014), *vol.* 756, *pp.* 689–715. © Cambridge University Press 2014
doi:10.1017/jfm.2014.451

Scaling behaviour in impulsively started viscous flow past a finite flat plate

Ling Xu[1] **and Monika Nitsche**[2,†]

[1]Department of Applied and Computational Mathematics and Statistics, University of Notre Dame, Notre Dame, IN 46556, USA

[2]Department of Mathematics and Statistics, University of New Mexico, Albuquerque, NM 87131, USA

(Received 10 September 2013; revised 13 June 2014; accepted 31 July 2014; first published online 4 September 2014)

Viscous flow past a finite flat plate which is impulsively started in the direction normal to itself is studied numerically using a high-order mixed finite-difference and semi-Lagrangian scheme. The goal is to resolve the details of the vorticity generation, and to determine the dependence of the flow on time and Reynolds number. Vorticity contours, streaklines and streamlines are presented for a range of times $t \in [0.0002, 5]$ and Reynolds numbers $Re \in [250, 2000]$, non-dimensionalized with respect to the driving velocity and the plate length. At early times, the starting vortex is small relative to the plate length and is expected to grow as if an external length scale were absent. We identify three different types of scaling behaviours consistent with this premise. (i) At early times, solutions with different values of Re are identical up to rescaling. (ii) The solution for fixed Re satisfies a viscous similarity law in time, locally in space, as illustrated by the core vorticity maximum, the upstream boundary layer thickness, and the maximum speed, in three different regions of the flow. (iii) The vortex core trajectory and the shed circulation satisfy inviscid scaling laws for several decades in time, and are consequently essentially Re-independent at these times. In addition, the computed induced drag and tangential forces are found to follow approximate scaling laws that define their dependence on time and Re.

Key words: vortex flows, vortex shedding

1. Introduction

Vorticity separation in flow past sharp edges is a fundamental process of intrinsic interest in fluid dynamics. The boundary layer vorticity is convected around the edge, where it concentrates and forms a vortex. The vortex grows in strength and size, eventually causing the boundary layers to separate as a shear layer that rolls up in a spiral shape around the vortex core. The starting vortex flow has been the focus of many experimental, analytical and numerical studies, beginning with the work of Prandtl (see Lugt 1995). This paper concerns flow past a finite flat plate of zero thickness which is impulsively started in the direction normal to itself. Closely related laboratory experiments include the works of Pierce (1961), Taneda & Honji (1971), Pullin & Perry (1980), Lian & Huang (1989) and Lepage, Leweke & Verga (2005).

†Email address for correspondence: nitsche@math.unm.edu

They visualize the rolled-up layer and yield data on the vortex size, core trajectory, core vorticity distribution and the onset of an instability along the outer spiral turns. Related numerical results include the simulations of Wang (2000) and Eldredge (2007) for viscous flow past thin rounded plates, those of Hudson & Dennis (1985), Dennis *et al.* (1993) and Koumoutsakos & Shiels (1996) for flow past finite plates of zero thickness, and Luchini & Tognaccini (2002), who studied flow past a semi-infinite plate of zero thickness. These works report vortex fields, vortex core trajectories and induced forces at intermediate to relatively large times.

The main goal here is to complement these earlier works with numerical simulations that resolve details of the vorticity evolution, and determine the flow dependence on time and Reynolds number. The flow is difficult to compute because of the singular geometry and unbounded initial velocities and vorticities, which necessitate a fine mesh and easily cause numerical instabilities. Here, we use a split method in time in which advection is treated using a semi-Lagrangian scheme, diffusion is treated with a three-level Crank–Nicholson method, and all finite difference and interpolation approximations are of fourth order. The method uses ideas from several previous works, including Staniforth & Côté (1991), E & Liu (1996), Johnston & Krasny (2002), Luchini & Tognaccini (2002), Seaid (2002) and Nitsche, Taylor & Krasny (2003). It is of second order for the present highly singular flow.

The flow is non-dimensionalized with respect to the driving velocity and the plate length. Well-resolved results are obtained for a range of times, $t \in [0.0002, 5]$, and several Reynolds numbers $Re = 250, 500, 1000, 2000$. The results give detailed information on the vorticity generation near the plate tip. For example, the recirculation region associated with the starting vortex and the corresponding region of opposite-signed vorticity are formed immediately after the start of the motion, while the local vorticity maximum in the vortex core is formed at a later time. We present the evolution of vorticity contours, particle streaklines and streamlines, and compute the vortex trajectory, shed circulation and induced plate forces, as a function of time and Re. The results are compared with experimental results of Pullin & Perry (1980) and numerical results of Koumoutsakos & Shiels (1996).

At early times, when the vortex size is small relative to the plate length, the flow is expected to behave like flow past a semi-infinite plate, and satisfy corresponding scaling laws. Here, we identify three types of scaling laws. (i) For viscous flow past a semi-infinite plate, one can eliminate the dependence on Re by appropriately rescaling length and time, see for example Luchini & Tognaccini (2002). As a result, the evolution in time with fixed Re equals the solution with variable Re at a fixed time, up to scale. We show that this scaling is well satisfied in the finite plate case, at small times. (ii) Several viscous flows with no external length scale are described by a self-similar function of time and a viscous length scale. In the present flow we find three regions, namely the upstream boundary layer, the vortex core, and the region of maximum flow speed, in which the viscous similarity law is satisfied, locally in space. (iii) Inviscid separation of a vortex sheet past a semi-infinite plate is known to grow self-similarly in time, globally in space (Pullin 1978). We find that the viscous vortex core trajectory and circulation satisfy the inviscid scaling for several decades in time. A consequence is that at these times, these quantities are basically Re-independent. In addition, the computed induced drag and tangential forces are found to follow approximate scaling laws that define their dependence on time and Re.

The results form a basis of comparison to evaluate for example lower order models for separation, such as inviscid point vortex models (e.g. Cortelezzi & Leonard 1993; Michelin & Llewellyn Smith 2009; Ysasi, Kanso & Newton 2011;

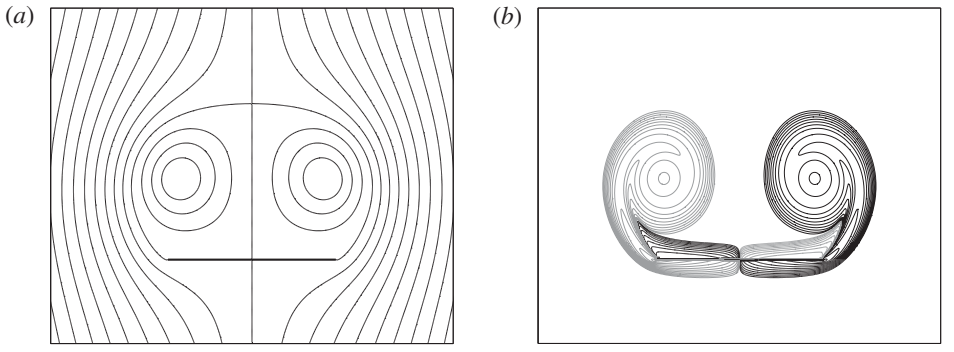

FIGURE 1. Sample solution at a relatively large time. (*a*) Streamlines. (*b*) Vorticity field. Positive vorticity contours are shown in black, negative ones in grey.

Wang & Eldredge 2013), or vortex sheet models (e.g. Krasny 1991; Nitsche & Krasny 1994; Jones 2003; Jones & Shelley 2005; Shukla & Eldredge 2007; Alben & Shelley 2008), the effect of the shape of the plate tip (Schneider *et al.* 2014), or the effect of the wedge angle in flow past wedges (Pullin & Perry 1980).

The paper is organized as follows. Section 2 describes the problem of interest and the governing equations. Section 3 describes the three types of viscous and inviscid scaling laws that hold for flow past a semi-infinite plate. Section 4 presents the numerical method, its accuracy and the resolution obtained. The numerical results are given in § 5: § 5.1 discusses the evolution for fixed Re; § 5.2 presents the dependence of the flow on Re and shows that at early times, solutions with variable Re are identical up to rescaling; § 5.3 presents three regions in which the solution with fixed Re locally satisfies viscous self-similar behaviour; § 5.4 presents the inviscid self-similar growth of the vortex core trajectory and circulation; and § 5.5 presents forces tangent to the plate and drag forces normal to it, as well as their apparent scaling. The results are summarized in § 6.

2. Problem formulation

2.1. *Problem description*

A finite plate of length L and zero thickness immersed in viscous fluid is impulsively started from zero velocity to a constant velocity $U > 0$ in the direction normal to itself. The flow is non-dimensionalized using L and L/U as the characteristic length and time scales. The flow is assumed to be two-dimensional. It is described in non-dimensional Cartesian coordinates $\boldsymbol{x} = (x, y)$, and time t, with fluid velocity $\boldsymbol{u}(\boldsymbol{x}, t) = (u(x, y, t), v(x, y, t))$. We choose a reference frame moving with the plate, in which the plate is positioned horizontally on the x-axis, centered at the origin, at

$$S = \{(x, y) : x \in [-\tfrac{1}{2}, \tfrac{1}{2}], y = 0\}, \tag{2.1}$$

the plate velocity is zero, and the far field velocity points upwards,

$$\boldsymbol{u}_\infty(t) = (0, 1). \tag{2.2}$$

To illustrate, figure 1 plots the streamlines and vorticity field at some relatively large time past the start of the motion. Here and throughout the paper, positive vorticity

contours are shown in black and negative contours in grey. The flow is assumed to remain symmetric about $x=0$, since at the times considered here, symmetry breaking instabilities are not expected to significantly affect the flow. Hereafter, results are only shown for the right half-plane, $x \geqslant 0$. The flow is driven by the potential flow induced by the far-field velocity, with stream function

$$\psi_\infty(\boldsymbol{x}) = \mathrm{Im}\left(\sqrt{\tfrac{1}{4}-z^2}\right), \tag{2.3}$$

where $z = x + \mathrm{i}y$.

2.2. *Governing equations*

The fluid flow is modelled by the incompressible Navier–Stokes equations with constant density. The governing equations, given in terms of the fluid vorticity $\omega(\boldsymbol{x}, t) = v_x - u_y$ and stream function $\psi(\boldsymbol{x}, t)$, are

$$\frac{\partial \omega}{\partial t} + (\boldsymbol{u}\cdot\boldsymbol{\nabla})\omega = \frac{1}{Re}\nabla^2\omega, \tag{2.4a}$$

$$\nabla^2\psi = -\omega, \quad \text{with } \psi = 0 \text{ on } S \text{ and } \psi \to \psi_\infty \text{ as } |\boldsymbol{x}| \to \infty, \tag{2.4b}$$

$$\boldsymbol{u} = \boldsymbol{\nabla}^\perp\psi, \quad \text{with } \boldsymbol{u} = 0 \text{ on } S, \tag{2.4c}$$

where $\boldsymbol{\nabla}^\perp\psi = (\partial\psi/\partial y, -\partial\psi/\partial x)$, $Re = LU/\nu$ and ν is the kinematic fluid viscosity.

3. Scaling at early times

At early times, when the starting vortex is much smaller than the size of the plate, the flow evolution is expected to be largely independent of the plate length and comparable with flow past a semi-infinite plate. Indeed, near the tip $z = x + \mathrm{i}y \approx 1/2$, the potential driving flow around the finite plate equals potential flow around a semi-infinite plate, to highest order,

$$\psi_\infty(\boldsymbol{x}) = \mathrm{Im}\sqrt{\frac{1}{4}-z^2} \approx \mathrm{Im}\sqrt{\frac{1}{2}-z} = \sqrt{r}\cos\left(\frac{\theta}{2}\right), \tag{3.1}$$

where $z - 1/2 = r\mathrm{e}^{\mathrm{i}\theta}$. In dimensional variables, which will be denoted by a hat throughout the paper,

$$\widehat{\psi}_\infty(\widehat{\boldsymbol{x}}) = UL\cdot\mathrm{Im}\sqrt{\frac{1}{4}-z^2} \approx a\sqrt{\widehat{r}}\cos\left(\frac{\theta}{2}\right), \tag{3.2}$$

where $\widehat{r} = Lr$ and $a = U\sqrt{L}$. The absence of an external length scale in the semi-infinite case implies that scaling laws hold, both in viscous and inviscid flow. Next, we describe three types of scaling laws for the semi-infinite flow that are observed in the present finite plate flow.

3.1. *Viscous scaling with variable Re*

Consider the Navier–Stokes equations (2.4) governing viscous flow around a semi-infinite plate on the negative x-axis, $S = \{(x, 0) \mid x \in (-\infty, 0]\}$, driven by $\psi_\infty(\boldsymbol{x}) = \mathrm{Im}(\mathrm{i}\sqrt{z})$. Let $\omega(\boldsymbol{x}, t; Re)$, $\psi(\boldsymbol{x}, t; Re)$ be the solution at time $t > 0$ with

Reynolds number Re. Then, for any value of τ, the pair (ω', ψ') defined by

$$\omega'(\boldsymbol{x}, t; Re) = \tau\omega\left(\tau^{2/3}\boldsymbol{x}, \tau t; \frac{Re}{\tau^{1/3}}\right), \quad \psi'(\boldsymbol{x}, t; Re) = \frac{1}{\tau^{1/3}}\psi\left(\tau^{2/3}\boldsymbol{x}, \tau t; \frac{Re}{\tau^{1/3}}\right), \tag{3.3a,b}$$

also solves (2.4) with the same boundary condition, $\psi' \to \mathrm{Im}(\mathrm{i}\sqrt{z})$ as $|\boldsymbol{x}| \to \infty$. This implies that one can recover the solution at time t with one value of Re from the solution with another $Re' = Re/\tau^{1/3}$ at another time $t' = \tau t$. Consequently, knowing the solution for one Re at all times yields the full solution for any other Re. This is equivalent to the fact shown by Luchini & Tognaccini (2002), that under appropriate rescaling the Navier–Stokes equations for flow past a semi-infinite plate reduce to Re-independent equations. We will show that the finite plate flow studied here satisfies the scaling (3.3) at early times.

3.2. *Viscous scaling in time with fixed Re*

For several viscous flows in which an external length scale is absent, the dimensional flow stream function is of the form

$$\widehat{\psi}(\widehat{\boldsymbol{x}}, \widehat{t}) = a(\nu\widehat{t})^{1/4} f\left(\frac{\widehat{x}}{\sqrt{\nu\widehat{t}}}, \frac{\widehat{y}}{\sqrt{\nu\widehat{t}}}\right). \tag{3.4}$$

Examples are a diffusing plane vortex sheet and flow past plane walls (Sherman 1990). For such flows the boundary or shear layer thickness, the fluid velocity and the vorticity scale as

$$\left.\begin{aligned} \widehat{\delta} \sim \sqrt{\nu\widehat{t}}, \quad & \delta \sim \sqrt{\frac{t}{Re}}, \\ \widehat{u} \sim a(\nu\widehat{t})^{-1/4}, \quad & u \sim \left(\frac{t}{Re}\right)^{-1/4}, \\ \widehat{\omega} \sim a(\nu\widehat{t})^{-3/4}, \quad & \omega \sim \left(\frac{t}{Re}\right)^{-3/4}. \end{aligned}\right\} \tag{3.5}$$

Here, the left-hand side gives the scaling in dimensional form, the right-hand side gives the corresponding non-dimensional form using the fact that $a = U\sqrt{L}$. We will show that for flow past a plate, the stream function is locally of the form (3.4) in different regions of the flow. In particular, we identify one of the scalings in (3.5) in each of three regions: the upstream boundary layer midway between the plate tip and the axis, a region of maximal flow speed near the shear layer, and a region near the vortex core.

3.3. *Inviscid scaling in time*

A model for inviscid separation past a flat plate consists of a vortex sheet attached to the plate tip that approximates the separated shear layer. In the absence of an external length scale, the inviscid vortex sheet roll-up is self-similar. The corresponding scaling laws for a semi-infinite free vortex sheet were first derived by Kaden (1931). Pullin (1978) considered vortex sheet separation at the edge of a semi-infinite plate, derived the associated similarity laws, and computed the self-similar vortex sheet shape. For

impulsively started background flow, the scaling laws for the spiral centre coordinates and the total sheet circulation are

$$\left.\begin{array}{ll} \widehat{x}_c, \widehat{y}_c \sim (a\widehat{t})^{2/3}, & x_c, y_c \sim t^{2/3}, \\ \widehat{\Gamma} \sim a^{4/3}\widehat{t}^{\,1/3}, & \Gamma \sim t^{1/3}. \end{array}\right\} \tag{3.6}$$

Again, the right-hand side lists the scaling in non-dimensional variables. We will show that the viscous vortex core trajectory and circulation satisfy the inviscid scaling (3.6).

4. Numerical approach

This section presents the numerical method used to solve (2.4) for viscous flow past the finite pate. Section 4.1 describes the numerical algorithm, § 4.2 presents the convergence rates and parameters used.

4.1. *Numerical method*

The method is based on fourth-order finite-difference approximations on a regular grid, and a semi-Lagrangian treatment of convection. The computational domain is the rectangular region

$$D = [0, x_{max}] \times [y_{min}, y_{max}], \tag{4.1}$$

with symmetry imposed across $x = 0$. The domain interior is given by the interior of $D \backslash S$, where S is the plate position (2.1). The computational boundary is $\partial D \cup S$. Here, $x_{max} > 1/2$, $y_{min} < 0$, $y_{max} > 0$ are chosen sufficiently large so that the vorticity ω effectively vanishes on ∂D for all times computed. The domain is discretized by $(N_x + 1) \times (N_y + 1)$ equally spaced gridpoints (x_i, y_j), where

$$x_i = ih, \quad i = 0, \ldots, N_x, \, h = x_{max}/N_x, \tag{4.2a}$$

$$y_j = y_{min} + jk, \quad j = 0, \ldots, N_y, \, k = (y_{max} - y_{min})/N_y, \tag{4.2b}$$

and N_x, N_y are chosen so that $h = k$. Similarly, time is discretized as

$$t_n = n\Delta t, \quad n = 0, \ldots, N, \, \Delta t = T_{fin}/N, \tag{4.2c}$$

where $T_{fin} = t_N$ is the final time. Stream function, velocity and vorticity are carried on the gridpoints, with $\psi^n_{i,j}$, $(u, v)^n_{i,j}$ and $\omega^n_{i,j}$ approximating $\psi(x_i, y_j, t_n)$, $(u, v)(x_i, y_j, t_n)$ and $\omega(x_i, y_j, t_n)$.

The boundary stream function at time t^n is ψ^n_{bd}. On the plate, $\psi_{bd} = 0$. This ensures that $v = 0$ on the plate. The values of ψ_{bd} on the remaining boundary ∂D are obtained by integration, using the domain-specific Green's function, see Step 1*b* below. The boundary vorticity at time t^n is ω^n_{bd}. On ∂D, $\omega_{bd} = 0$. The values of ω_{bd} on the remaining boundary, the upstream and downstream sides of the plate S, are denoted by ω^n_+ and ω^n_-, respectively, and obtained by enforcing $u = 0$ on the plate, see Step 1*d* below. The initial condition is given by zero vorticity in the domain interior.

The vorticity at time t_n is updated to time t_{n+1} by solving (2.4) in two steps.

Step 1: The interior vorticity is convected by solving

$$\frac{\mathrm{D}Q}{\mathrm{D}t} = 0 \quad \text{subject to} \quad Q(t_n) = \omega^n, \tag{4.3a}$$

for one timestep and setting $\omega^* = Q(t_{n+1})$. The values of ω^* are then used to obtain updated interior and boundary values of the stream function, velocity and vorticity, ψ^{n+1}, $(u, v)^{n+1}$ and ω_{bd}^{n+1}.

Step 2: The interior vorticity is diffused by solving the equation

$$\frac{\partial Q}{\partial t} = \frac{1}{Re}\nabla^2 Q \quad \text{subject to} \quad Q(t_n) = \omega^*, \quad Q_{bd}(t^{n+1}) = \omega_{bd}^{n+1}, \tag{4.3b}$$

for one timestep and setting $\omega^{n+1} = Q(t_{n+1})$.

Several details in each of the two steps above remain to be explained.

Step 1*a*: Equation (4.3*a*) is solved using a semi-Lagrangian scheme which is second order in time and fourth order in space, as follows. For each interior grid point (x_i, y_j), first find the location of a particle at t_n that travels with the fluid velocity, and ends up at (x_i, y_j) at t_{n+1}. This is equivalent to solving

$$\frac{\mathrm{d}\boldsymbol{x}}{\mathrm{d}t} = \boldsymbol{u}(\boldsymbol{x}, t), \quad \boldsymbol{x}(t_{n+1}) = (x_i, y_j), \tag{4.4a,b}$$

for $\boldsymbol{x}(t_n)$, where $\boldsymbol{x} = (x, y)$. Equation (4.4) is solved to second order in time using velocity values at the current and previous timestep, $(u, v)^{n-1}$ and $(u, v)^n$. Then, obtain the vorticity of the particle at t_n, $\omega(\boldsymbol{x}(t_n), t_n)$, from vorticity values at nearby grid points using a fourth-order bi-cubic interpolant. Finally, set $\omega_{i,j}^* = \omega(\boldsymbol{x}(t_n), t_n)$. Further details can be found in Xu (2012).

Step 1*b*: Updated interior values of the stream function at t_{n+1} are obtained by solving

$$\nabla^2 \psi^{n+1} = \omega^* \quad \text{in interior}, \quad \psi = \psi_{bd}^{n+1} \quad \text{on } \partial D \cup S, \tag{4.5a,b}$$

which is discretized using a compact fourth-order finite-difference scheme (Strikwerda 1989, equation (12.5.6)). The resulting linear system for ψ_{ij}^{n+1} is solved using the conjugate gradient method. The required boundary values ψ_{bd} are zero on the plate S and on the axis, $x = 0$. On the remaining three sides of ∂D, ψ_{bd} is computed by integration,

$$\psi_{bd}(\boldsymbol{x}_{bd}, t) = \psi_\infty(\boldsymbol{x}_{bd}, t) + \int_{D/S} \omega(\boldsymbol{x}, t) G_S(\boldsymbol{x}_{bd}, \boldsymbol{x})\, \mathrm{d}\boldsymbol{x}, \tag{4.6a}$$

where

$$G_S(\boldsymbol{x}, \boldsymbol{x}_o) = \log \left| \frac{\sqrt{\dfrac{z - 1/2}{z + 1/2}} - \sqrt{\dfrac{z_o - 1/2}{z_o + 1/2}}}{\sqrt{\dfrac{z - 1/2}{z + 1/2}} - \sqrt{\dfrac{z_o - 1/2}{z_o + 1/2}}^*} \right| \tag{4.6b}$$

is the domain-specific Green's function for the Laplace operator, $z = x + \mathrm{i}y$, $z_o = x_o + \mathrm{i}y_o$ and $*$ denotes the complex conjugate. The integral is computed using the fourth-order Simpson's method, where we sum only over those points with $|\omega| \geqslant 10^{-9}$. The values of ψ_∞ are induced by a vortex sheet in place of the plate whose strength is such that no flow passes through the plate. Instead of using (2.3), we approximate ψ_∞ using a sufficiently fine discretization of the vortex sheet, following the approach taken by Nitsche & Krasny (1994). This method can be applied to other geometries as well, even if the analytic expression for the potential is not known.

Step 1*c*: Updated interior values of velocity at t_{n+1} are obtained by solving

$$(u, v)^{n+1} = \nabla^{\perp}\psi^{n+1} \tag{4.7}$$

using the fourth-order centred difference approximations. Boundary values of velocity are only needed on the plate, where they vanish, and on the axis $x = 0$, where they are obtained by centred differences from ψ^{n+1} and use of symmetry. The updated velocity is used at the next timestep, in Step 1*a*.

Step 1*d*: Updated boundary vorticity values on the plate at t_{n+1} are obtained from the updated stream function by enforcing the no-slip boundary condition. The boundary condition $\psi = 0$ ensures that $v = 0$ on the walls. The boundary vorticity is

$$\omega_{bd}^{n+1} = -\frac{\partial^2\psi^{n+1}}{\partial y^2}. \tag{4.8}$$

This equation is discretized so that $\psi = 0$ and $\partial\psi/\partial y = 0$ on the wall, and therefore $u = 0$. Here, we use a fourth-order version of the Thomas formula, known as Briley's formula, following E & Liu (1996, (their (2.11))). The updated vorticity values are used in Step 2, below, as well as at the next timestep, in Step 1*a*.

Step 2: Equation (4.3*b*) is solved by discretizing the Laplace operator with the fourth-order compact finite difference scheme also used for (4.5) and then applying an implicit Crank–Nicolson method which is second order in time and fourth order in space (Fletcher 1991, p. 255ff). The resulting linear system for the vorticity ω^{n+1} is solved using the conjugate gradient method.

This completes the description of the numerical method. In order to visualize flow streaklines, particles are initially placed near the plate tip and transported by the fluid flow. Their position $\boldsymbol{x}(t)$ is given by

$$\frac{\mathrm{d}\boldsymbol{x}}{\mathrm{d}t} = \boldsymbol{u}(\boldsymbol{x}, t), \quad \boldsymbol{x}(0) = \boldsymbol{x}_o, \tag{4.9a,b}$$

where $\boldsymbol{u}$ is the fluid velocity. The velocity at the current particle position is obtained by interpolation, and the equation is solved using the second-order explicit Adams–Bashforth scheme, for a range of initial positions.

4.2. *Resolution and convergence*

To test this numerical scheme, Xu (2012) applied it to the driven cavity problem of E & Liu (1996), and reproduced their results. For smooth cavity lid motion the method was confirmed to converge to fourth order in space, and to first order in time. The slow convergence in time is a property of standard splitting schemes. Here, we discuss the performance of the method applied to the more singular case of impulsively started flow past a sharp edge.

To illustrate the effect of resolution, figure 2 plots vorticity contours computed for $Re = 500$ at $t = 0.05$, with various values of the meshsize h and timestep Δt. The resolution is coarsest in figure 2(*a*), finest in figure 2(*d*), as given in the caption. The figure shows contours $\omega = \pm 2^j$, $j = -5, \ldots, 12$, in a region close to the plate tip, with positive vorticity in black, negative vorticity in grey. The zero vorticity contour level appears as a thick dark curve which in fact consists of many positive and negative vorticity contour levels of small magnitude. Recall that the background driving velocity flows from bottom (upstream) to top (downstream). This causes the

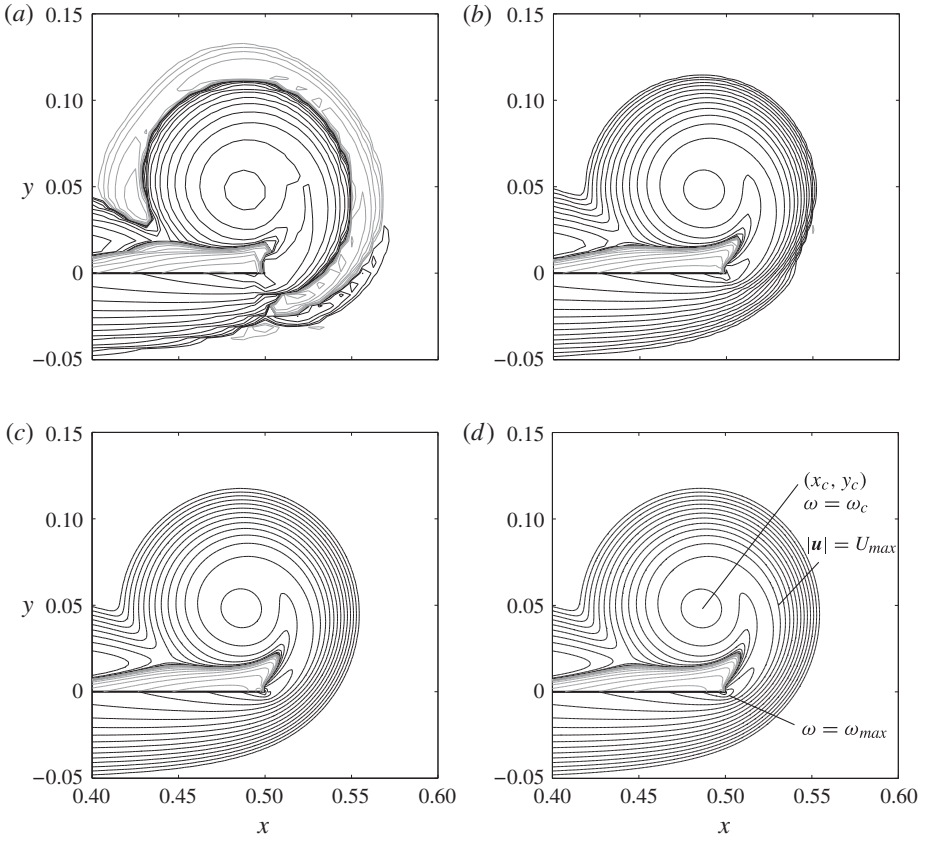

FIGURE 2. Vorticity contours $\omega = \pm 2^j$, $j = -5, \ldots, 12$ at $t = 0.05$ for $Re = 500$, computed with (*a*) $h = 1/160$, $\Delta t = 4 \times 10^{-4}$, (*b*) $h = 1/320$, $\Delta t = 2 \times 10^{-4}$, (*c*) $h = 1/640$, $\Delta t = 1 \times 10^{-4}$ and (*d*) $h = 1/1280$, $\Delta t = 5 \times 10^{-5}$.

formation of a boundary layer of positive vorticity around the right half-plate. The maximum vorticity, ω_{max}, occurs near the tip of the plate, one gridpoint away from it, at all times, as indicated in figure 2(*d*). At the time shown here, positive vorticity has been convected to form a shear layer that has separated from the tip and rolled up into a vortex on the downstream side of the plate. The vortex has a second local maximum in the core vorticity, at (x_c, y_c) with magnitude ω_c. It induces positive flow on the downstream plate wall, which causes the formation of a thin region of opposite signed, negative vorticity along the wall. For later reference the figure also shows the point of maximum flow speed, U_{max}, which occurs just outside the first turn of the separated shear layer.

If h, Δt are too large, as in figure 2(*a*), the lack of resolution is evidenced by alternate layers of positive and negative vorticity that form outside the starting vortex. If the flow is only slightly underresolved, as in figure 2(*b*), ripples in the vorticity are first visible below and to the right of the tip. With increasing resolution, as in figure 2(*c*), the ripples disappear and the vorticity is smooth. Finer resolution, as in figure 2(*d*), leaves the results practically unchanged.

We found this to be the case at all times computed: at all times, an instability is apparent for large enough values of h, Δt. If the resolution is sufficiently fine, the

h	Δt	T_{fin}	$[x_{min}, x_{max}] \times [y_{min}, y_{max}]$
1/160	(4–5) $\times 10^{-4}$	5	$[0, 2] \times [-0.50, 5.50]$
1/320	2×10^{-4}	0.5–3	$[0, 1] \times [-0.25, 0.75]$
1/640	(0.5–2) $\times 10^{-4}$	0.2–0.6	$[0, 0.75] \times [-0.25, 0.50]$
1/1280	(2–5) $\times 10^{-5}$	0.05–0.1	$[0, 0.75] \times [-0.25, 0.50]$
1/2560	(4–5) $\times 10^{-6}$	0.005–0.038	$[0, 0.55] \times [-0.05, 0.10]$
1/5120	2×10^{-6}	0.001–0.005	$[0, 0.55] \times [-0.05, 0.10]$

TABLE 1. Mesh size h, timestep Δt, final time T_{fin}, and computational domain used in the computations, for the range of $Re \in [250, 2000]$. For a given value of h, the smaller values of Δt and larger final times T_{fin} are used for the larger values of Re.

h	e_c^h	e_ω^h	$e_{\psi,x}^h$ Along $x = 0.5$	$e_{\psi,y}^h$ Along $y = 0.048$
1/160	3.51×10^{-3}	8.30×10^{-3}	0.0155	0.005 811
1/320	1.80×10^{-3}	1.83×10^{-3}	0.0060	0.002 386
1/640	1.86×10^{-4}	4.19×10^{-5}	0.0010	0.000 683

TABLE 2. Errors e_ω^h, e_c^h, $e_{\psi,x}^h$, and $e_{\psi,y}^h$, at $t = 0.05$, computed with $Re = 500$.

results are smooth and remain unchanged to the eye under further refinement. The values of h, Δt required for smooth results are smaller at earlier times. We thus take the following approach: results at a given time are computed with a value of h, Δt sufficiently small so that the vorticity contours with $|\omega| \geqslant 2^{-5}$ appear resolved. Table 1 lists the meshsizes and timesteps used in time intervals $[0, T_{fin}]$, for different values of T_{fin}. The range given for Δt and T_{fin} reflects values used for different Reynolds numbers Re. For larger Re, a given time requires a smaller value of h and Δt. For example, $h = 1/320$ is used for the runs with $T_{fin} = 0.5$ for $Re = 250$, but is required for much larger $T_{fin} = 3$ for $Re = 2000$.

An estimate of the order of convergence is obtained from table 2. The table lists the errors in the position $\boldsymbol{x}_c^h = (x_c^h, y_c^h)$ and vorticity magnitude ω_c^h of the vortex core at $t = 0.05$ (see figure 2*d*), as well as errors in the stream function along horizontal and vertical lines near the vortex core. Here, $\boldsymbol{x}_c^h$ and ω_c^h are obtained by interpolation. The errors are computed relative to the results with $h = 1/1280$, as follows

$$e_\omega^h = \frac{|\omega_c^h - \omega_c^{1/1280}|}{|\omega_c^{1/1280}|}, \quad e_c^h = \frac{\|\boldsymbol{x}_c^h - \boldsymbol{x}_c^{1/1280}\|_2}{\|\boldsymbol{x}_c^{1/1280}\|_2} \tag{4.10a}$$

$$e_{\psi,x}^h = \|\psi^h - \psi^{1/1280}\|_\infty \quad \text{along } x = 0.5 \tag{4.10b}$$

$$e_{\psi,y}^h = \|\psi^h - \psi^{1/1280}\|_\infty \quad \text{along } y = 0.048. \tag{4.10c}$$

The data in table 2 is summarized in figure 3, together with a line with slope $m = 2$. Even though the amount of data points is rather limited, the data is consistent with second order or better rate of convergence, with faster convergence away from the tip.

5. Numerical results

We now present the numerical results for the finite-plate flow. Section 5.1 describes the evolution in time for fixed $Re = 500$. Sections 5.2–5.4 illustrate the three types

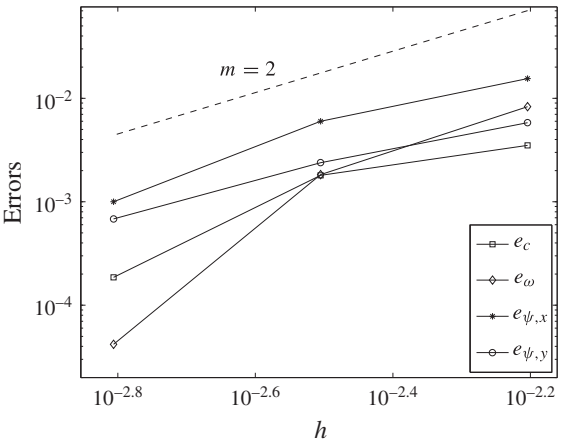

FIGURE 3. Errors e^h_c, e^h_ω, $e^h_{\psi,x}$, $e^h_{\psi,y}$, versus h, as indicated. A line of slope $m = 2$ is also shown.

of scalings (3.3)–(3.6) observed in the flow. Section 5.5 presents the induced forces tangent and normal to the plate.

5.1. *Evolution for* $Re = 500$

Figure 4 shows the evolution computed for $Re = 500$. It shows vorticity contours (left column), streaklines (middle column) and streamlines (right column) at the indicated times. At each time, the results plotted are computed with the finest resolution listed in table 2 for that time. The vorticity contours are $\omega = \pm 2^j$, $j = -5, \ldots, 12$, with positive contours in black, negative ones in grey.

Initially, the driving flow generates a boundary layer of positive vorticity along both the upstream and downstream sides of the plate. Upstream vorticity is convected downstream, concentrating near the tip as a vortex that is already visible at the earliest time shown here, $t = 0.005$. The vortex entrains nearby vorticity, while vorticity further away is swept away by the background flow, thus depleting the region in between. As a result, the leading vorticity, which is initially connected to the downstream boundary layer, begins to separate from it. At some time between $t = 0.2$ and 0.5, the positive vorticity contours shown in the starting vortex have completely separated from the positive boundary layer vorticity, resulting in a more clearly defined starting vortex.

The starting vortex induces a region of recirculating flow that can be seen in the corresponding streamlines. The recirculation region forms immediately after the motion begins. The fluid inside the recirculation region, near the wall, flows in the direction opposite to the starting flow, generating a boundary layer of negative vorticity. The negative vorticity is barely visible in the figure at $t = 0.005$, but grows and is clearly seen at later times. It is noteworthy that in our computations, the recirculation region and associated negative vorticity is visible already at time $t = O(\Delta t)$, within the first 10 timesteps, indicating that it forms immediately after the start of the motion. Luchini & Tognaccini (2002) suggest that the initial stage in viscous separation, referred to as the Rayleigh stage, is one in which the flow is potential everywhere except for a thin viscous boundary layer of constant thickness around all of the plate, including the plate tip. Our results indicate that the Rayleigh stage is absent for impulsively started flow. Indeed, simulations of accelerated flows

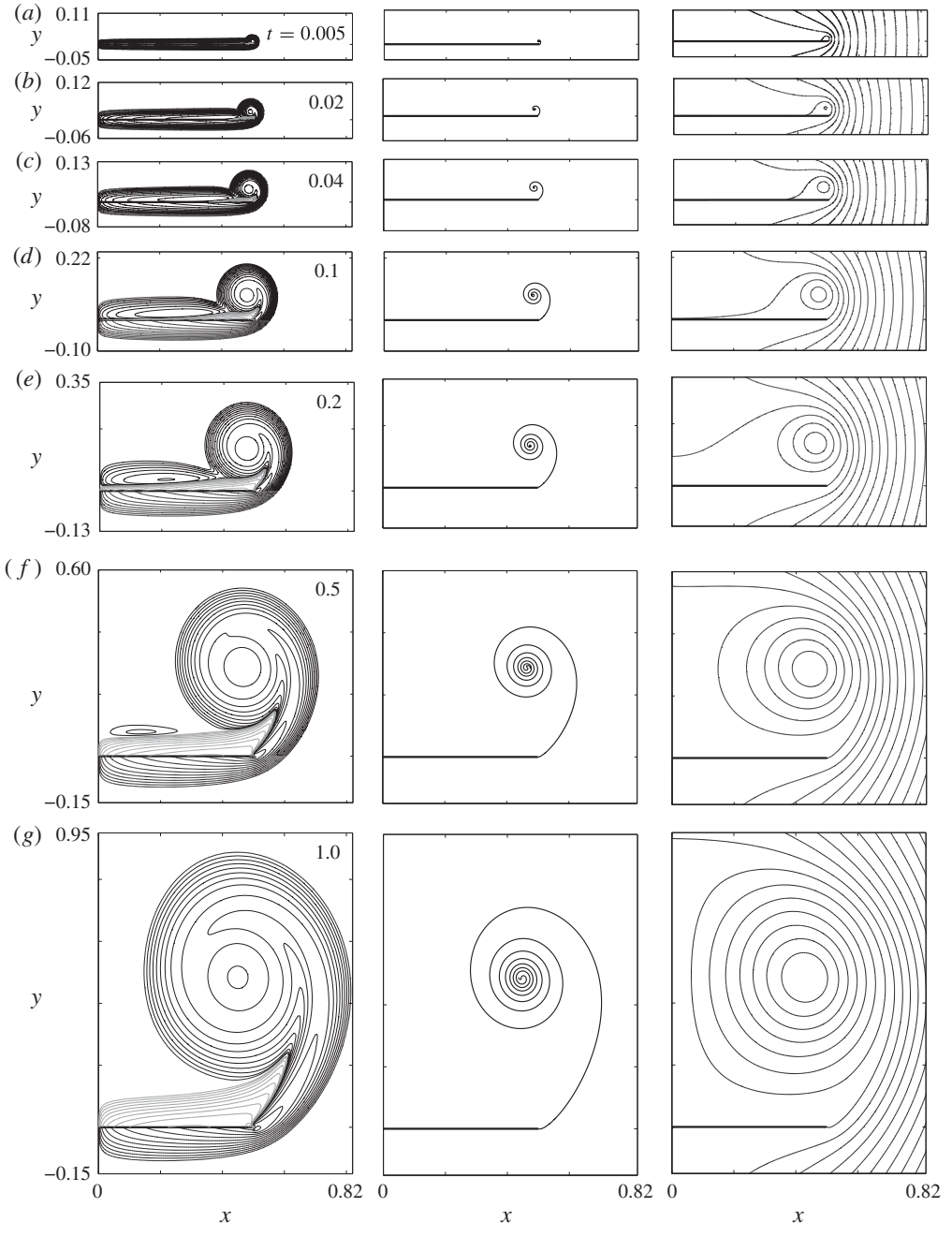

FIGURE 4. For caption see next page.

with plate velocities Ut^p show that for $p > 0$, the Rayleigh layer around the tip is present during an initial time interval, but that the length of this time interval shrinks to zero as $p \to 0$ (Xu & Nitsche 2014).

As the starting vortex grows, the negative vorticity region grows horizontally along the plate and is also stretched and entrained into the starting vortex. Around time $t = 3$,

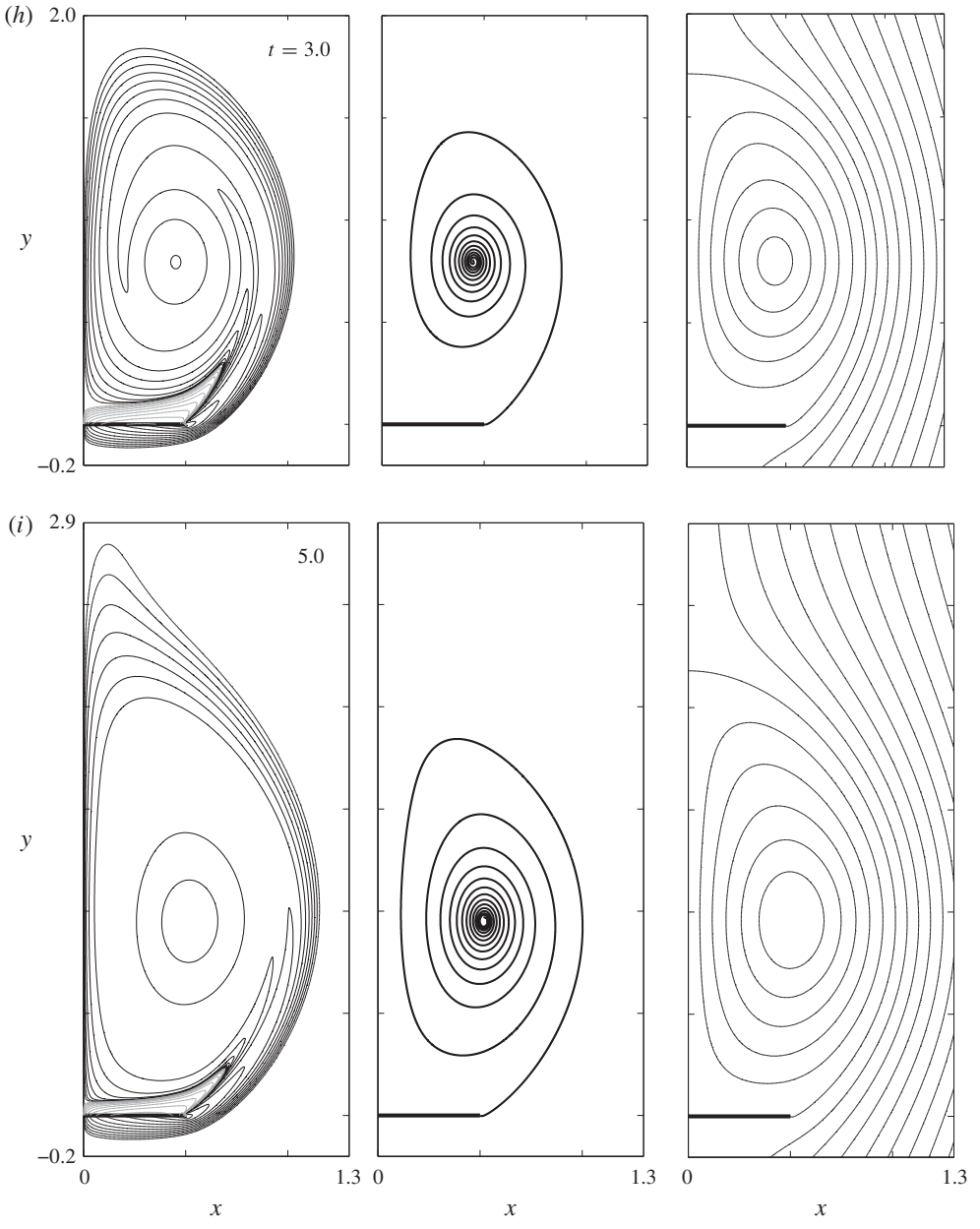

FIGURE 4. (cntd). Vorticity, streaklines and streamlines, for $Re = 500$ at a sequence of times, $t = 0.005$, 0.02, 0.04, 0.1, 0.2, 0.5, 1.0, 3.0, 5.0, as indicated. The vorticity contour levels are $\omega = \pm 2^j$, $j = -5, \ldots, 12$. The stream function levels are $\psi = -1{:}0.05{:}1$ for $t \leqslant 1$ and $\psi = -1{:}0.1{:}1$ for $t = 3, 5$.

the positive vorticity in the starting vortex has reached the axis of symmetry, $x = 0$. It diffuses out of the recirculation region, so that at $t = 5$, much vorticity is outside the enclosing streamline and moves upwards away from the plate. The results at the larger times presented here are in good agreement with results shown by Koumoutsakos & Shiels (1996).

The streaklines, shown in the middle column of figure 4, are obtained by releasing a particle at a point near the tip at each timestep, and evolving it with the fluid velocity. At a given time, the figure shows the position of all particles at that time that were released previously, thus mimicking what is observed in an experiment if dye is continuously released at a point near the tip. Each released particle circulates around the vortex centre, with particles that were released earlier traveling closer to the centre. This gives the streaklines a spiral shape. The spiral tightens near the centre and the number of spiral turns increases in time. The maximum vorticity near the plate tip is convected with the particles along the streakline, and diffuses. Thus, the streakline is a good indicator of the centreline of the separated shear layer. At the times shown, the spiral centre is also a good indicator of the vorticity maximum in the vortex core. The overall vortical region, and the recirculation region, extend beyond the region occupied by the spiral.

The streamlines, in the right column, show the recirculation region. This region is enclosed by the $\psi = 0$ streamline, which leaves the plate tip and, at small times, reattaches on the downstream side, at a short distance behind the vortex. As the recirculation region grows, the enclosing streamline $\psi = 0$ first reaches the axis, between time $t = 0.1$ and 0.2, and then continues to move up along the centreline, $x = 0$. It then forms the familiar rounded symmetric recirculation bubble downstream of the plate, as observed experimentally and computationally, before the flow loses its symmetry at later times (see, e.g., Van Dyke, 1982, figure 64; Koumoutsakos & Shiels, 1996, figure 18).

Figure 5 plots a closeup of the vorticity contours near the plate tip, as well as two flow streamlines, shown as dashed curves. One is the $\psi = 0$ streamline enclosing the recirculation region, the other is a closed streamline near the centre of rotation. Figure 5(*a*) shows that very early, at $t = 0.0002$, the recirculation region is already well-formed, with a well-defined rotation center, and associated negative vorticity region. Positive vorticity has begun to concentrate downstream, near the plate tip, but it does not yet have a local vorticity maximum that could identify a vortex core. Thus, this early on, the rotation centre exists, but the core vorticity maximum does not. Figure 5(*b*), which plots the solution a little later, at $t = 0.0016$, shows a local vorticity maximum emerging within the recirculation region. This local maximum remains well defined and grows in time, as shown in figure 5(*c*,*d*). As time increases, the centre of rotation and the position of the vorticity maximum are in better agreement.

5.2. *Viscous scaling for variable Re*

This section shows the solution at a fixed time for variable *Re* and the extent to which it mimics the evolution in time for fixed *Re*. Figure 6 plots vorticity contours, streamlines and streaklines at $t = 1$ for $Re = 250$, 500, 1000, 2000. As *Re* increases, the vorticity contours show well-known features: the wall boundary layer thickness decreases; the separated shear layer thickness decreases, and its spiral roll-up becomes more evident; the thickness of the negative vorticity region decreases. For larger *Re*, the separated vorticity is supported in a smaller, more compact region. Some dependence on *Re* is also observed in the spiral streaklines, and in the streamlines. Most noticeably, the spiral roll-up near the centre is tighter for larger *Re*, with more spiral turns, and the streamline density within the vortex increases, indicating larger fluid velocities.

The scaling (3.3) that holds for flow past a semi-infinite plate implies that the dependence on *Re* at a fixed time reflects the evolution in time for fixed *Re*.

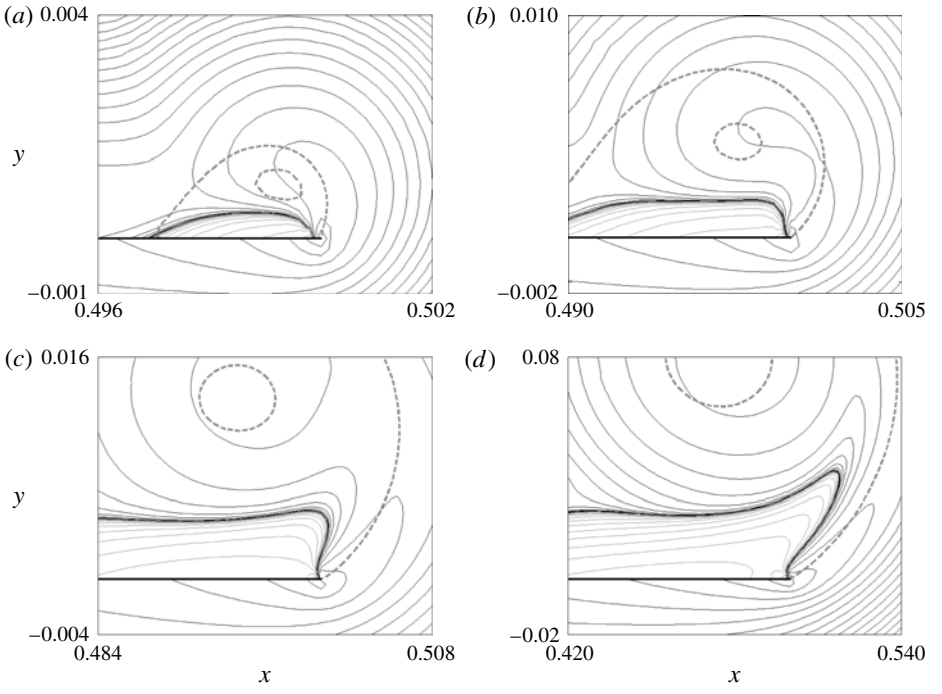

FIGURE 5. Closeup of vorticity contours near the plate tip, for $Re = 500$, at (*a*) $t = 0.0002$, (*b*) $t = 0.0016$, (*c*) $t = 0.008$ and (*d*) $t = 0.1$. Vorticity contour levels are $\pm 2^j$, $j = -8, \ldots, 15$. The dashed curves are streamlines.

At early times, the present results are consistent with that scaling. To illustrate, figure 7 plots two sequences of solutions. The left column shows the solution at a fixed time $t = 0.005$ using an increasing sequence of Reynolds numbers Re, at the given location x. The right column shows the solution using a fixed Reynolds number $Re' = Re/\tau^{1/3} = 500$ at an increasing sequence of times $t' = \tau t$, at location $x' - 1/2 = \tau^{2/3}(x - 1/2)$. These values are chosen to correspond to the left column, according to the scaling (3.3), for $\tau = 1/8, 1, 8, 64$. The figure shows that at early times, the results on the right agree with the left, showing that the solution for different Re, left, can be recovered from the time series, right. At the last time shown on the right, $t = 0.32$, the finite length scale becomes evident and differences appear. For example, the vortex center coordinate y_c is larger on the right than on the left, at $t = 0.005$.

We illustrate a sample application of the observed scaling. Figure 5 shows that for $Re = 500$, the vorticity maximum in the vortex core appears around $t = 0.0016$. Based on the scaling (3.3), one can predict that for any other Re, the vorticity maximum appears at $t \approx 0.0016(500/Re)^3 \approx (58/Re)^3$, as long as this time is sufficiently small.

5.3. *Viscous scaling in time for fixed Re*

Here, we present three regions in space, in which the viscous scaling in time for fixed Re, (3.4), is locally approximately satisfied. The three regions are illustrated in figure 8(*a*), on top of contours of the flow speed $|\boldsymbol{u}|$. These contours are dense wherever velocity gradients are large. Therefore, areas of large vorticity such as the

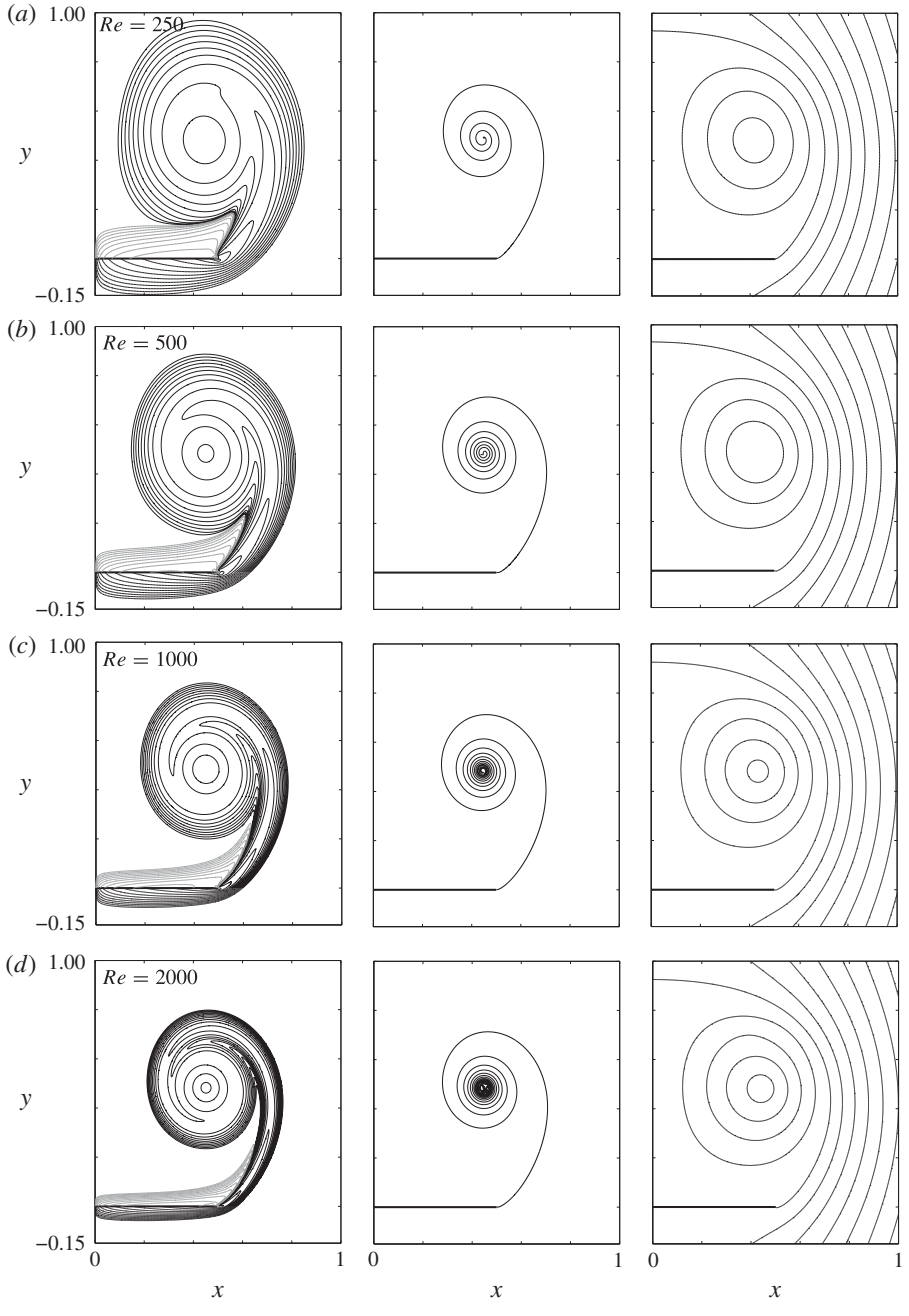

FIGURE 6. Vorticity, streaklines and streamlines at $t = 1$ for $Re = 250$, 500, 1000 and 2000 (*a–d*). Contour levels are $\pm 2^j$, $j = -5, \ldots, 12$ (vorticity) and $-1{:}0.1{:}1$ (stream function).

boundary layer, the separated shear layer, and the vortex centre appear darker. The flow speed has a local minimum at the vortex centre, in region 'd'. Its absolute maximum occurs in region 'c', at a point just to the right of the outermost shear layer turn. Region 'b' contains a portion of the upstream boundary layer.

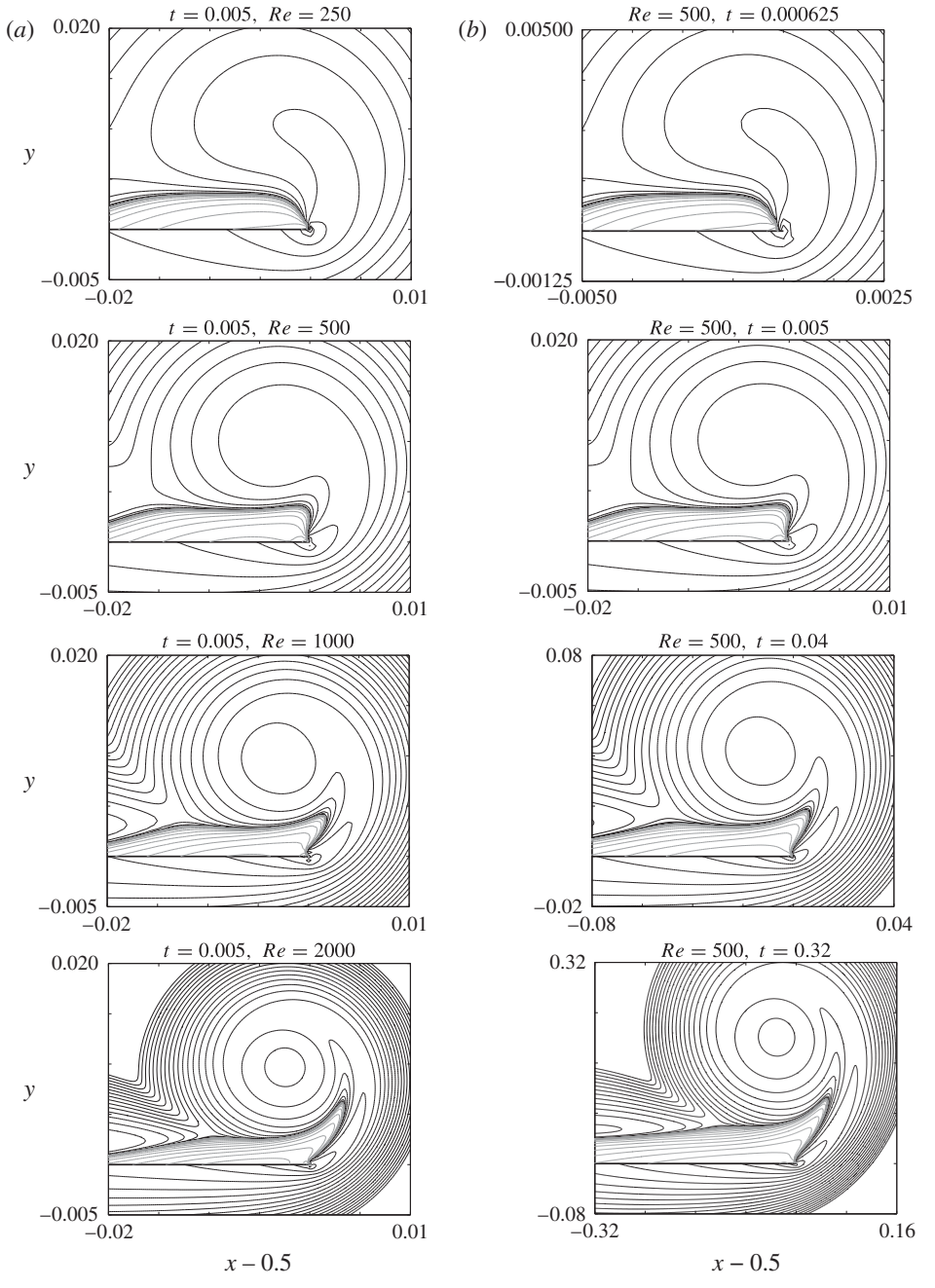

FIGURE 7. Vorticity contours near the plate tip: (*a*) solution at a fixed time $t = 0.005$, for increasing values of Re; (*b*) solution for fixed $Re = 500$, at an increasing sequence of times.

Each of figure 8(*b–d*) presents one quantity in each of the three regions. Figure 8(*b*) plots the boundary layer thickness δ measured in region 'b' on the upstream side of the plate. The value of δ is measured at $x = 0.2$, as the thickness of the region below the plate with $\omega \geqslant 2^{-5}$. Figure 8(*c*) plots the maximum speed U_{max}, which

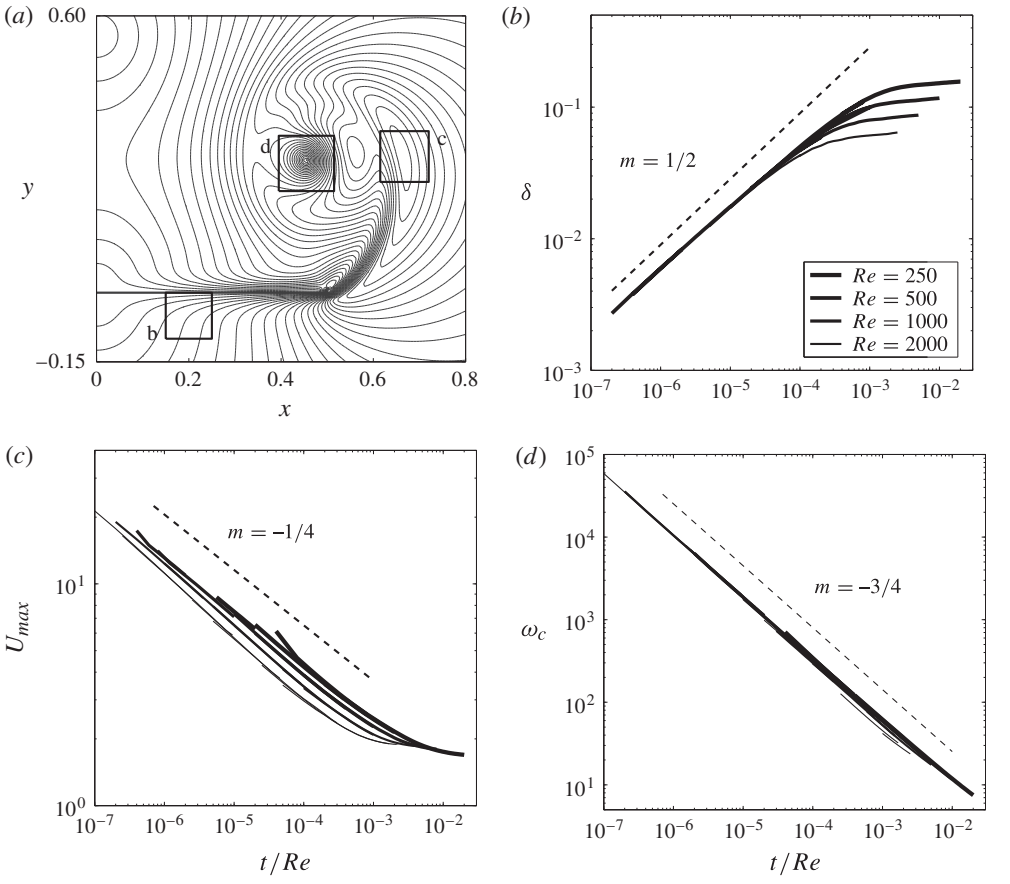

FIGURE 8. (*a*) Contour plot of flow speed $|\boldsymbol{u}|$, showing three regions in the domain. (*b*) Upstream boundary layer thickness δ, at $x = 0.2$, in region 'b'. (*c*) Maximum speed U_{max}, in region 'c'. (*d*) Core vorticity ω_c, in region 'd'. Results are plotted versus t/Re, for all $Re = 250$, 500, 1000 and 2000, as indicated in (*b*).

occurs in region 'c'. Figure 8(*d*) plots the maximum core vorticity $\omega_c = \omega(x_c, y_c)$ in region 'd'. All quantities are plotted versus t/Re. All subplots in figure 8 plot the results for all Re computed, as indicated in the legend in figure 8(*b*), and all values of h used, as given in table 2. Thus, each subplot shows results for approximately 20 different time series, computed with different Re and resolutions. The values show remarkably little dependence on the resolution and, for each value of Re, collapse onto one curve that is linear in the logarithmic scale, over a large portion of the computed time interval, with the indicated slopes. In addition, the values in figure 8(*b*,*d*) are completely independent on Re over much of the times computed. The quantities satisfy

$$\delta \approx 6\left(\frac{t}{Re}\right)^{1/2}, \quad U_c \approx 0.4\left(\frac{t}{Re}\right)^{-1/4}, \quad \omega_c \approx 0.335\left(\frac{t}{Re}\right)^{-3/4}, \tag{5.1a–c}$$

over four to five decades in t/Re, clearly displaying the scaling (3.4) locally, in their corresponding regions. In the case of U_{max}, the scaling is less well satisfied for the larger values of Re. Most likely, this is because U_{max} occurs at a point just outside the

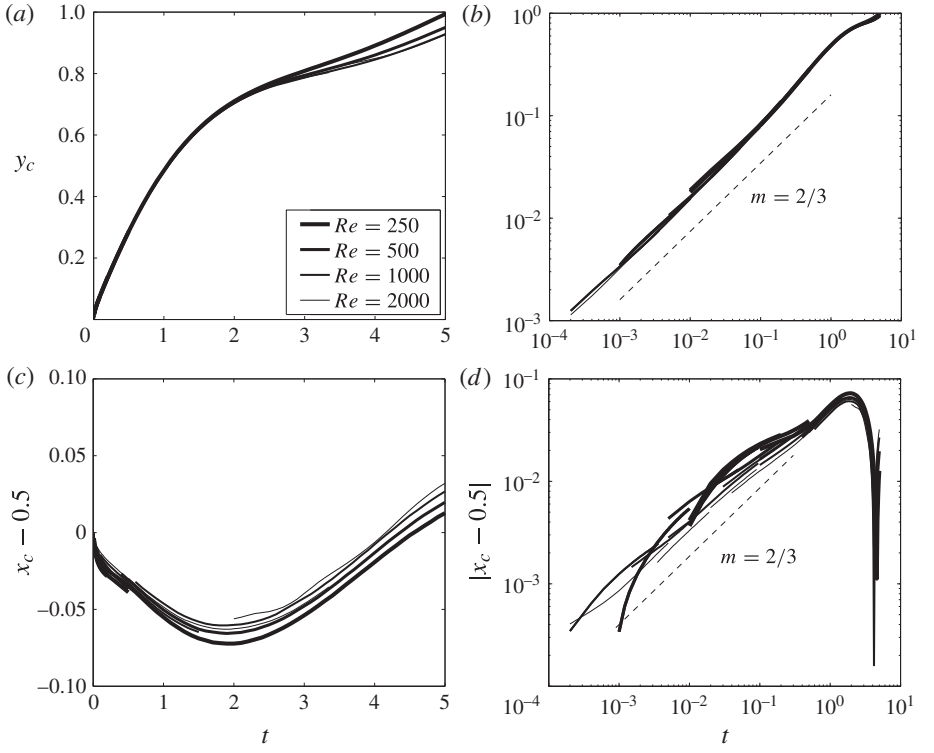

FIGURE 9. Core trajectory for $Re = 250, 500, 1000, 2000$, as indicated. (*a*,*b*) Vertical core position y_c versus t. (*c*,*d*) Horizontal core displacement $x_c - 0.5$ from edge. The dashed lines have the indicated slopes.

shear layer centreline. We conclude that the scaling (3.4) is well satisfied in regions 'b', 'd', but only approximately so in 'c'.

5.4. *Inviscid scaling in time*

This section presents the behaviour in time of the vortex core trajectory and circulation and shows that initially, they satisfy the inviscid scaling inherent to vortex sheet separation at the edge of a semi-infinite plate, and are therefore practically independent of the value of Re.

5.4.1. *Vortex trajectory*

The vortex core coordinates are defined as the coordinates (x_c, y_c) at the vorticity maximum ω_c. They are defined only after this maximum away from the plate tip has formed. As mentioned in § 5.2, as a result of the viscous scaling (3.3), this occurs earlier for higher Re, at a time $t \sim 1/Re^3$. We note that alternatively, the core position can be defined as the centre of rotation, which exists at all times in the impulsively started case considered in this paper. However, we did not explore this option here.

Figure 9 plots x_c and y_c versus t, computed for all Re, as indicated in the legend in figure 9(*a*), and all values of h used, as given in table 2. Thus, as in figure 8, each subplot in figure 9 shows approximately 20 different time series, computed with different Re and resolutions. Figure 9(*a*,*b*) plots the vertical displacement y_c of the

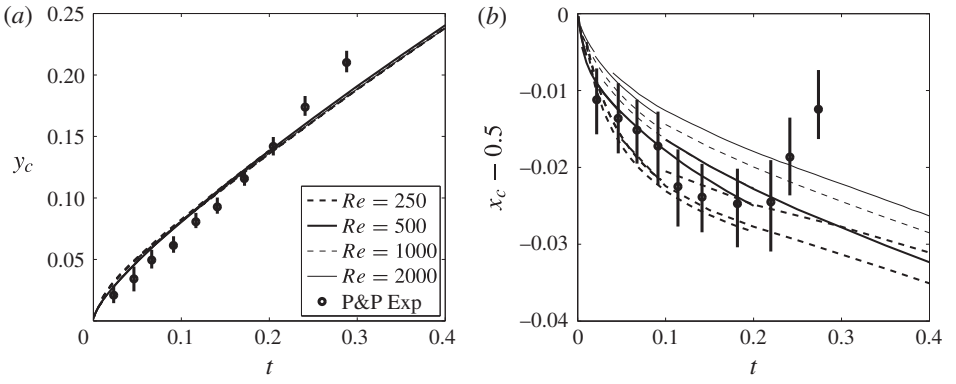

FIGURE 10. Comparison of vortex core coordinate with experimental data of Pullin & Perry (1980). (*a*) Vertical displacement y_c. (*b*) Horizontal displacement $x_c - 0.5$. Computed data for all Reynolds number and experimental data are shown, as indicated in the legend. The vertical bars through the experimental data are the error bars indicated in P&P.

vortex core from the plate, on a linear and a logarithmic scale, respectively. Here, the values for all Re and all resolutions computed collapse onto one curve, with no apparent dependence on h, and only a small dependence on Re visible at later times. On the logarithmic scale, the curve is well approximated by a line with slope 2/3, for about three to four decades in time.

Figure 9(*c*) plots the horizontal displacement $x_c - 0.5$ of the vortex core from the plate, on a linear scale. It shows that $x_c - 0.5$ is initially negative. Up to about $t = 2$, the symmetric vortices at each end of the plate move slightly inward, as would be the case in the self-similar inviscid case. After that time they begin moving outwards, reflecting the growing vorticity of the opposite signed vortex at the other end of the plate. As a result, at the final time computed, the vortex has moved past the edge of the plate, with $x_c > 0.5$. Figure 9(*d*) plots the absolute displacement $|x_c - 0.5|$, on a logarithmic scale. These values are an order of magnitude smaller than those of y_c, and less well resolved, with the dependence on h more visible. However, to within the available resolution, the results depend little on Re. The logarithmic scale shows that for about three decades, the data is also approximately linear with slope 2/3. The figure thus shows that for three to four decades,

$$x_c - 0.5 \approx -0.1t^{2/3}, \quad y_c \approx 0.37t^{2/3}. \tag{5.2a,b}$$

This scaling agrees with the self-similar inviscid vortex sheet spiral roll-up (3.6).

Pullin & Perry (1980) measured vortex core positions in a laboratory experiment of flow past wedges. They reported data at quite small times, giving a good basis of comparison for our present numerical results. Figure 10 reproduces their results for the smallest wedge considered, of wedge angle $\beta = 5°$, together with our computed results for the flat plate, for all Re. The experimental data span an early time interval $t \in [0, 0.3]$. The computed values of y_c are in quite good quantitative agreement with the experimental measurements. For the better resolved lower-Reynolds-numbers cases, our computed values of $x_c - 0.5$ agree with the experimental data, except for the last two data points. The experimental data were obtained at larger Reynolds number of $Re \approx 6000$, but the data is expected to be practically independent of Re, as in the case of y_c. Thus, the variability in the computed values of x_c is attributed to insufficient

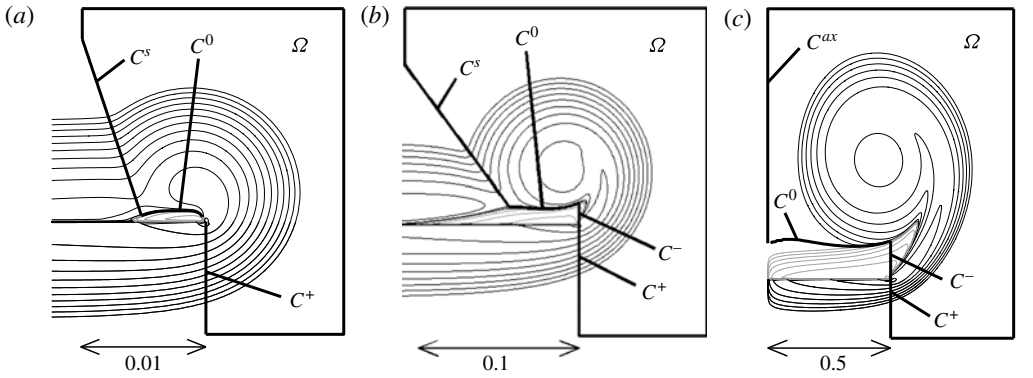

FIGURE 11. Sketch defining the domain Ω at (*a*) early times, (*b*) intermediate times, (*c*) late times, and portions of its boundary with non-zero circulation flux, $C^{\pm}$ (upstream and downstream components across plate tip), C^s (slant), C^0 (zero vorticity) and C^{ax} (axis).

resolution. We cannot explain the deviation of the computation from the last two experimental data points in figure 10(*b*).

5.4.2. *Vortex circulation*

Not much data is available in the literature on the shed circulation at early times in viscous flows. This is in part because it is not clear *a priori* how to define the shed circulation at times when the starting vortex is not clearly distinguished from the boundary layer vorticity. Here, we follow the work in Nitsche & Xu (2014) and define the shed circulation, normalized by LU, to be

$$\Gamma = \int_{\Omega(t)} \omega \, \mathrm{d}A, \tag{5.3}$$

where the region $\Omega(t)$ is defined as shown in figure 11. The region is defined slightly differently in different time regimes of the flow, with continuous transitions between them. At early times, when the region of negative vorticity has not yet been entrained past the vertical line $x = 0.5$, we follow the sketch in figure 11(*a*). On the upstream side ($y < 0$), the region Ω is bounded by the vertical line through the tip, C^+. On the downstream side ($y > 0$), it is bounded by the zero vorticity contour C^0 that separates negative from positive vorticity, and by a slant line C^s through points of high curvature visible in the vorticity contours. That is, the region Ω is defined to include all vorticity to the right of the tip, to exclude the negative boundary layer vorticity, and is limited on the left by the slant line. Figure 11(*b*) shows the vorticity at intermediate times, when the negative vorticity on the downstream side has been entrained past the vertical line $x = 0.5$. Here, we include all vorticity, positive or negative, to the right of the vertical line through the tip, which introduces a vertical piece of boundary C^- above the plate. Figure 11(*c*) shows the vorticity at later times, when all of the positive boundary layer vorticity on the downstream wall is entrained into the vortex. At this time the vortex is bounded on the left not by the slant line, but by the axis C^{ax}. Each subplot in figure 11 shows a typical length scale, indicating that the three regimes in time span three decades of length scales in space.

Nitsche & Xu (2014) studied the effect of viscosity on the circulation shedding rates. They found that the major contribution to the circulation is inviscid convection

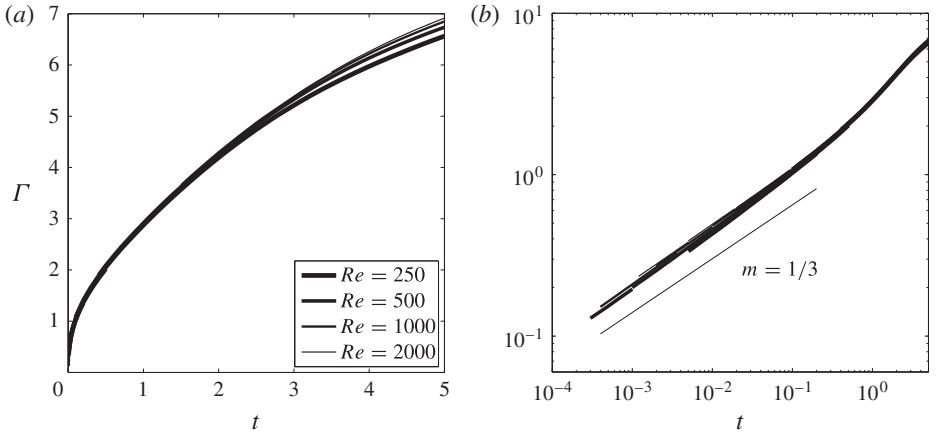

FIGURE 12. Circulation $\Gamma(t)$ for $Re = 250, 500, 1000, 2000$. ($a$) Linear scale. ($b$) Logarithmic scale.

of vorticity into Ω through C^+. Furthermore, their results show that at early times the total shed circulation is highly independent of Re. However, viscous diffusion of vorticity out of Ω through $C^0 \cup C^-$ is significant, adding a non-negligible contribution to $\Gamma(t)$. The apparent contradiction that viscous diffusion is significant, but independent of the value of Re, is attributed to the fact that the amount of diffusion depends on

$$\frac{1}{Re}\int_{\partial\Omega} \nabla\omega \cdot \boldsymbol{n}\, \mathrm{d}s, \tag{5.4}$$

and at early times, larger values of Re yield proportionally larger vorticity gradients.

Here, we report on the scaling of Γ. Figure 12(a,b) plots the shed circulation $\Gamma(t)$ computed using the above definition, on a linear and logarithmic scale, respectively. The data for all Re and all values of h used is shown, so that again, each subplot consists of approximately 20 runs, each with different parameters. The data is highly independent of Re over most of the times shown, with some dependence visible on the linear scale at late times. The logarithmic scale in figure 12(b) shows that Γ satisfies the scaling predicted by inviscid similarity theory (Pullin 1978) remarkably well, and satisfies

$$\Gamma(t) \approx 2t^{1/3}, \tag{5.5}$$

for about three decades in time. The data deviates from the self-similar scaling around $t \approx 0.2$, independently of Re. Finally, we note that, just like the data for ω_c and y_c, the computed circulation shows little dependence on the meshsize used in the computation. Even though the figure plots the results for all meshsizes and time intervals given in table 2, the data is an almost continuous function in time.

5.5. *Forces acting on plate*

The vorticity near the plate wall induces forces tangent and normal to the wall. This section presents the integral tangential and normal forces over the right half-plate, denoted by $F_\parallel$ and $F_\perp$. In our case, the normal force $F_\perp$ is the drag force parallel to the background flow. The tangential force $F_\parallel$ is normal to the background flow and generally referred to as lift. By symmetry, the overall lift over the whole plate is

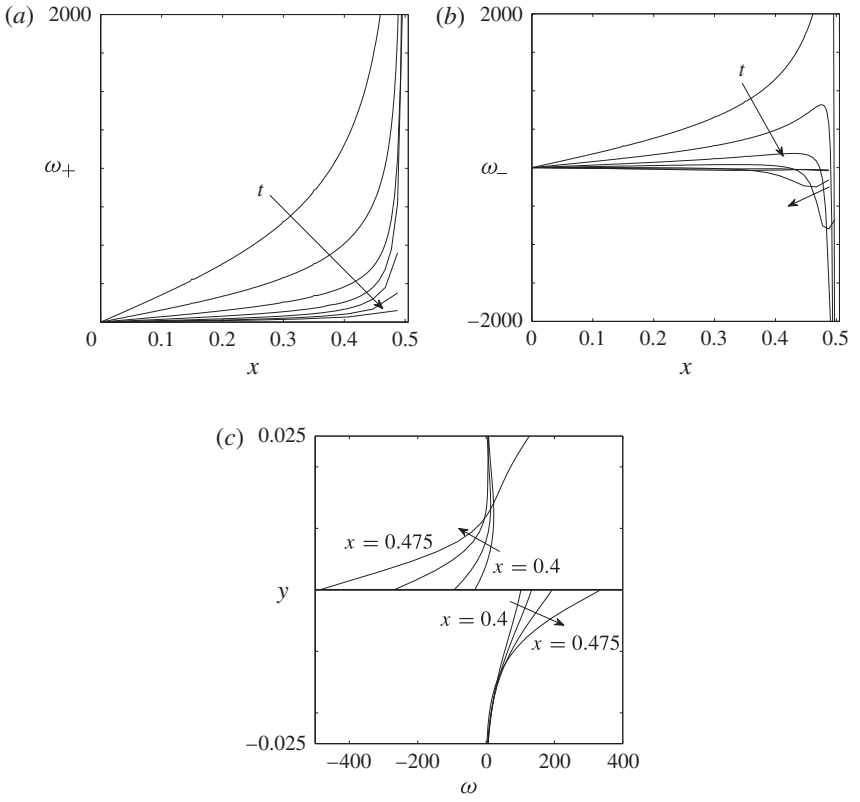

FIGURE 13. Vorticity near wall, for $Re = 500$. (a,b) Upstream and downstream wall vorticity ω_+ and ω_- versus x, at $t = 0.0002$, 0.001, 0.005, 0.02, 0.08, 0.5 and 3. (c) Vorticity ω at $t = 0.04$ along lines $x = 0.4$, 0.425, 0.45 and 0.475, versus y. The arrows indicate increasing t and x, respectively.

zero. The integral $F_\parallel$ over half the plate measures forces acting tangent to the plate in the outwards direction. Here, we compute the drag $F_\perp$ and the tangential force $F_\parallel$ following the formulation given by Eldredge (2007),

$$F_\parallel(t) = \frac{2}{Re}\int_0^{1/2} x\left[\frac{\partial\omega_+}{\partial y}(x,0,t) + \frac{\partial\omega_-}{\partial y}(x,0,t)\right]\mathrm{d}x, \tag{5.6a}$$

$$F_\perp(t) = \frac{2}{Re}\int_0^{1/2} \left[\omega_+(x,0,t) + \omega_-(x,0,t)\right]\mathrm{d}x, \tag{5.6b}$$

where all forces are normalized by $\rho U^2 L/2$. By symmetry, the total drag is $2F_\perp$.

These forces depend on the vorticity and vorticity gradients on the upstream and dowstream side of the plate wall. To illustrate, figure 13 shows the wall vorticity and vorticity gradients for $Re = 500$. Figure 13(a,b) plots the wall vorticity $\omega_\pm$ upstream and downstream of the plate, along the wall, as a function of x, at an increasing sequence of times, with arrows denoting the direction of increasing time. Figure 13(a) shows that on the upstream side, the vorticity is initially large and positive, and unbounded near the tip. As time increases the wall vorticity decreases. Figure 13(b) shows that on the downstream side, the vorticity is initially large and

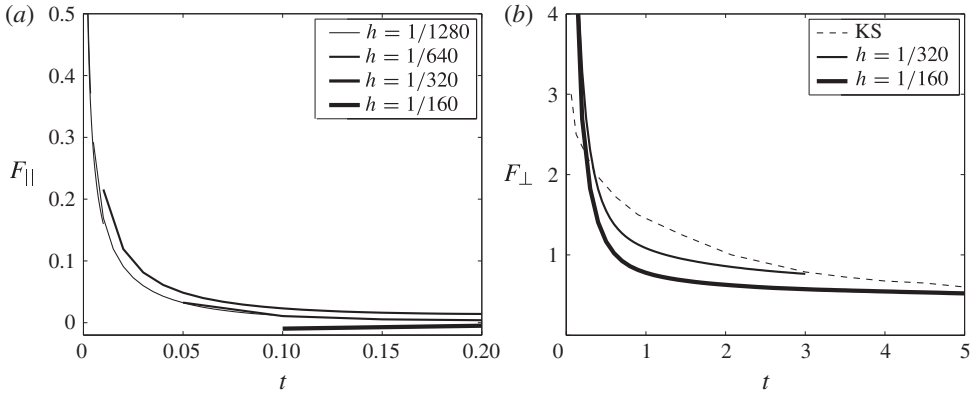

FIGURE 14. (*a*) Tangential force $F_\parallel$ and (*b*) drag $F_\perp$ for $Re = 1000$, versus t, computed with the indicated values of h. For comparison, (*b*) includes the data by Koumoutsakos & Shiels (1996, KS).

positive, but negative unbounded near the tip. As time increases the positive wall vorticity decreases but a region of negative wall vorticity grows. Figure 13(*c*) plots the vorticity at a fixed time along vertical cross-sections $x = \text{const.}$, as functions of y. It shows the negative vorticity above the plate, and shows that as x approaches the edge, the vorticity gradients $\partial\omega/\partial y$ at $y = 0$ increase.

The large values of the vorticity and its derivatives at early times and near the plate tip are difficult to compute accurately. As a result, computing the forces using formulation (5.6) is sensitive to discretization errors. To illustrate, figure 14 plots the computed lift and drag for $Re = 1000$ for various values of h and shows that the convergence in h is slow. An alternative formulation for the drag force is used by Koumoutsakos & Shiels (1996) (KS), who compute drag as the time derivative of an area integral, see their (40)–(41). The value of $F_\perp$ given by (5.6*b*) corresponds to the variable c_D plotted in KS in their figure 13. Figure 14(*b*) above compares the drag computed here with the values computed by KS, for $Re = 1000$. The figure shows that the values are in fairly good agreement, although differences exist, mainly in the decay rate at early times.

Figure 15(*a*,*b*) plots the drag and tangential forces on a logarithmic scale, for all Reynolds numbers computed here, and for all values of h used. They show that the results at early times collapse quite well onto a common curve that is approximately linear with slope $m \approx -1/2$. Note that the drag in figure 15(*a*) is plotted versus time t, while the tangential forces in figure 15(*b*) are plotted versus a scaled time $Re \cdot t$. The data indicates that at early times

$$F_\parallel(t) \approx (Re \cdot t)^{-1/2}, \quad F_\perp(t) \approx 6t^{-1/2}. \tag{5.7a,b}$$

These results suggest that at a fixed early time, the lift vanishes like $1/\sqrt{Re}$ as $Re \to \infty$, while the drag is largely independent of Re. In view of (5.7), this in turn indicates that the wall vorticity grows as $Re^{1/2}$, while the wall vorticity gradients grow faster, almost linearly in Re. At later times, the drag force decreases with increasing Re, consistent with the results shown by Dennis *et al.* (1993) and by KS.

While the observed approximate scaling is not explained by viscous or inviscid arguments, the results are consistent with the inviscid limit, in the following sense. In

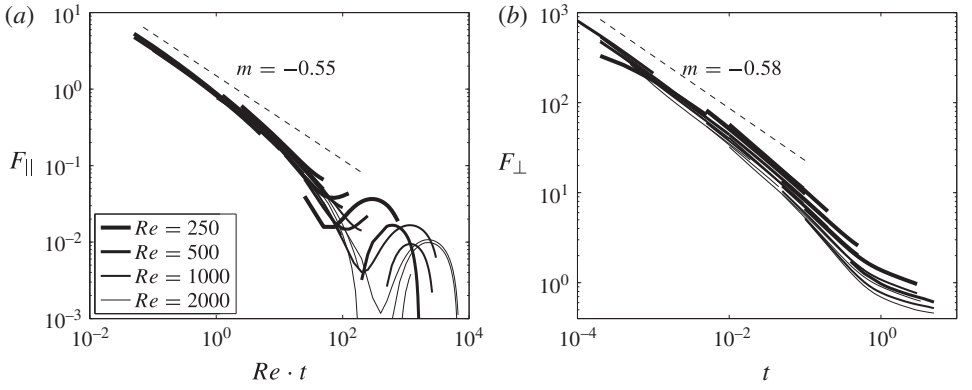

FIGURE 15. (*a*) Tangential force $F_{\parallel}$ versus $Re \cdot t$, (*b*) drag force $F_{\perp}$ perpendicular to wall versus t, for $Re = 250$, 500, 1000, 2000, as indicated in (*a*). The dashed lines have the indicated slopes.

the case of inviscid vortex sheet separation at the edge of the plate, the drag force is non-zero, while the tangential forces are absent, in agreement with the limit $Re \to \infty$ in (5.7), at fixed time t.

6. Summary

Viscous flow past a finite flat plate of zero thickness which is impulsively started in the direction normal to itself is studied using highly resolved numerical simulations, for a range of Reynolds numbers $Re \in [250, 2000]$ and a range of times $t \in [0.0002, 5]$. All variables are non-dimensionalized with respect to the driving velocity and the plate length. We present vorticity contours, particle streaklines, streamlines, the vortex trajectory and the shed circulation, and study the dependence of the solution on time and on Re.

Detailed information on the flow is found in particular on the early vortex formation period. The results reveal the time-scale at which vorticity concentrates at the tip: for the impulsively started flow, the recirculation region identifying a vorticity concentration forms immediately after the start of the motion. This implies that the Rayleigh stage, in which a thin viscous boundary layer of constant thickness surrounds the plate tip, is absent. On the other hand, a local vorticity maximum within the vortex core does not appear immediately after the start of the motion, but after some non-zero time.

The flow also satisfies scaling laws that hold asymptotically as $t \to 0$, and actually describe the computed flow well for several decades in time. At these times, the vortex size is small relative to the plate length, and the flow approximates flow past a semi-infinite plate. We identify three types of scaling laws consistent with the semi-infinite case. (i) The finite plate solutions for variable Re at early times approximately satisfy

$$\omega'(\boldsymbol{x}, t; Re) = \tau\omega\left(\tau^{2/3}\boldsymbol{x}, \tau t; \frac{Re}{\tau^{1/3}}\right), \tag{6.1}$$

for any value of τ. Thus, the evolution in time with fixed Re mimics the solution at a fixed time, with increasing Re. It follows, for example, that the local vorticity

maximum in the vortex core appears at $t \approx (58/Re)^3$. (ii) The solution for fixed Re is consistent with a dimensional stream function of the form

$$\widehat{\psi}(\widehat{\boldsymbol{x}}, \widehat{t}) = a(\nu\widehat{t})^{1/4} f\left(\frac{\widehat{x}}{\sqrt{\nu\widehat{t}}}, \frac{\widehat{y}}{\sqrt{\nu\widehat{t}}}\right), \tag{6.2}$$

locally, in certain regions of the flow. Namely, the boundary layer thickness on the upstream plate wall; the maximum core vorticity in the vortex core; and the maximum flow speed just outside of the separated shear layer, all closely satisfy the corresponding self-similar growth. (iii) The vortex core trajectory and shed circulation closely satisfy inviscid scaling laws,

$$x_c, y_c \sim t^{2/3}, \quad \Gamma \sim t^{1/3}, \tag{6.3a,b}$$

for approximately $t \leqslant 0.2$. During these times, they are largely independent of Re. In addition, the tangential forces and the drag force normal to the plate satisfy approximate scaling laws at early times. At these times, the tangential forces vanish as Re increases, while the drag depends little on Re.

The above scaling laws describe the flow dependence on time and Re at small times. The results presented here form a basis of comparison to evaluate simpler vortex shedding models, or the flow dependence on the shape of the plate. However, this is beyond the scope of this paper.

Acknowledgements

We thank the reviewers for helpful comments on this work. We are grateful to Professors S. Cowley, J. Eldredge, H. Johnston, R. Krasny and D. Pullin for many discussions and suggestions on several aspects of this work. M.N. also gratefully acknowledges S. Cowley for hosting her during a sabbatical visit at Cambridge University where some of this work was concluded.

REFERENCES

ALBEN, S. & SHELLEY, M. J. 2008 Flapping states of a flag in an inviscid fluid: bistability and the transition to chaos. *Phys. Rev. Lett.* **100**, 074301.

CORTELEZZI, L. & LEONARD, A. 1993 Point vortex model of the unsteady separated flow past a semi-infinted plate with transverse motion. *Fluid Dyn. Res.* **11**, 264–295.

DENNIS, S. C. R., QIANG, W., COUTANCEAU, M. & LAUNAY, J.-L. 1993 Viscous flow normal to a flat plate at moderate Reynolds numbers. *J. Fluid Mech.* **248**, 605–635.

E, W. & LIU, J. G. 1996 Essentially compact schemes for unsteady viscous incompressible flows. *J. Comput. Phys.* **126**, 122–138.

ELDREDGE, J. D. 2007 Numerical simulation of the fluid dynamics of 2D rigid body motion with the vortex particle method. *J. Comput. Phys.* **221**, 626–648.

FLETCHER, C. A. J. 1991 *Computational Techniques for Fluid Dynamics, Vol. 1*. Springer.

HUDSON, J. D. & DENNIS, S. C. R. 1985 The flow of a viscous incompressible fluid past a normal flat plate at low and intermediate Reynolds numbers: the wake. *J. Fluid Mech.* **160**, 369–383.

JOHNSTON, H. & KRASNY, R. 2002 Fourth-order finite difference simulation of a differentially heated cavity. *Intl J. Numer. Meth. Fluids* **40**, 1031–1037.

JONES, M. 2003 The separated flow of an inviscid fluid around a moving flat plate. *J. Fluid Mech.* **496**, 405–441.

JONES, M. A. & SHELLEY, M. J. 2005 Falling cards. *J. Fluid Mech.* **540**, 393–425.

KADEN, H. 1931 Aufwicklung einer unstabilen Unstetigkeitsfläche. *Ing.-Arch.* **2**, 140–179; (NASA Technical Translation: Curling of an unstable discontinuity surface, NASA-TT-F-14230, 51 p, 1971.) (English trans. R.A.Lib.Trans. no. 403).

KOUMOUTSAKOS, P. & SHIELS, D. 1996 Simulation of the viscous flow normal to an impulsively started and uniformly accelerated flat plate. *J. Fluid Mech.* **328**, 177–277.

KRASNY, R. 1991 Vortex sheet computations: roll-up, wakes, separation. *Lect. Appl. Maths* **28**, 385–402.

LEPAGE, C., LEWEKE, T. & VERGA, A. 2005 Spiral shear layers: roll-up and incipient instability. *Phys. Fluids* **17**, 031705.

LIAN, Q. X. & HUANG, Z. 1989 Starting flow and structure of the starting vortex behind bluff bodies with sharp edges. *Exp. Fluids* **8**, 95–103.

LUCHINI, P. & TOGNACCINI, R. 2002 The start-up vortex issuing from a semi-infinite flat plate. *J. Fluid Mech.* **455**, 175–193.

LUGT, H. J. 1995 *Vortex Flow in Nature and Technology*. Krieger Publishing Company.

MICHELIN, S. & LLEWELLYN SMITH, S. G. 2009 An unsteady point vortex method for coupled fluid–solid problems. *Theor. Comput. Fluid Dyn.* **23**, 127–153.

NITSCHE, M. & KRASNY, R. 1994 A numerical study of vortex ring formation at the edge of a circular tube. *J. Fluid Mech.* **276**, 139–161.

NITSCHE, M., TAYLOR, M. A. & KRASNY, R. 2003 Comparison of regularizations of vortex sheet motion. In *Computational Fluid and Solid Mechanics* (ed. K. J. Bathe), Elsevier Science.

NITSCHE, M. & XU, L. 2014 Circulation shedding in viscous starting flow past a flat plate. *Fluid Dyn. Res.* **46** (6, Part 2).

PIERCE, D. 1961 Photographic evidence of the formation and growth of vorticity behind plates accelerated from rest in still air. *J. Fluid Mech.* **11**, 460–464.

PULLIN, D. I. 1978 The large-scale structure of unsteady self-similar rolled-up vortex sheets. *J. Fluid Mech.* **88**, 401–430.

PULLIN, D. I. & PERRY, A. E. 1980 Some flow visualization experiments on the starting vortex. *J. Fluid Mech.* **97**, 239–255.

SCHNEIDER, K., PAGET-GOY, M., VEGA, A. & FARGE, M. 2014 Numerical simulation of flows past flat plates using volume penalization. *Comput. Appl. Math.* **33** (2), 481–495.

SEAID, M. 2002 Semi-Lagrangian integration schemes for viscous incompressible flows. *Comput. Meth. Appl. Maths* **2**, 392–409.

SHERMAN, F. S. 1990 *Viscous Flow*. McGraw-Hill.

SHUKLA, R. K. & ELDREDGE, J. D. 2007 An inviscid model for vortex shedding from a deforming body. *Theor. Comput. Fluid Dyn.* **21**, 343–368.

STANIFORTH, A. & CÔTÉ, J. 1991 Semi-Lagrangian integration schemes for atmospheric models – a review. *Mon. Weath. Rev.* **119**, 2206–2223.

STRIKWERDA, J. C. 1989 *Finite Difference Schemes and Partial Differential Equations*. Wadsworth and Brooks/Coles.

TANEDA, S. & HONJI, H. 1971 Unsteady flow past a flat plate normal to the direction of motion. *J. Phys. Soc. Japan* **30**, 262–272.

VAN DYKE, M. 1982 *An Album of Fluid Motion*. Parabolic Press.

WANG, Z. J. 2000 Vortex shedding and frequency selection in flapping flight. *J. Fluid Mech.* **410**, 323–341.

WANG, C. & ELDREDGE, J. D. 2013 Low-order phenomenological modeling of leading-edge vortex formation. *Theor. Comput. Fluid Dyn.* **27** (5), 577–598.

XU, L. 2012 Viscous flow past flat plates. PhD thesis, University of New Mexico.

XU, L. & NITSCHE, M. 2014 Start-up vortex flow past an accelerated flat plate (submitted) arXiv:1404.4585 [physics.flu-dyn].

YSASI, A., KANSO, E. & NEWTON, P. K. 2011 Wake structure of a deformable Joukowski airfoil. In *Fluid Dynamics: From Theory to Experiment*, vol. 240, pp. 1574–1582.